

RESEARCH LETTER

10.1002/2015GL066451

Key Points:

- Strongest magnetic anomalies are near Caloris impact basin
- Anomalies occur over smooth plains and probable Caloris ejecta
- Results are consistent with lunar orbital anomaly studies

Supporting Information:

- Supporting Information S1

Correspondence to:

L. L. Hood,
lon@lpl.arizona.edu

Citation:

Hood, L. L. (2015), Initial mapping of Mercury's crustal magnetic field: Relationship to the Caloris impact basin, *Geophys. Res. Lett.*, 42, 10,565–10,572, doi:10.1002/2015GL066451.

Received 4 OCT 2015

Accepted 29 NOV 2015

Accepted article online 11 DEC 2015

Published online 23 DEC 2015

Initial mapping of Mercury's crustal magnetic field: Relationship to the Caloris impact basin

L. L. Hood¹
¹Lunar and Planetary Laboratory, University of Arizona, Tucson, Arizona, USA

Abstract Seventy-eight low-altitude passes of Mercury Surface, Space ENvironment, GEochemistry, and Ranging magnetometer data from August to September of 2014 have been applied to produce an approximate map of the crustal magnetic field at a constant altitude of 80 km covering latitudes of 50°–80°N and longitudes of 160°–330°E. The strongest anomalies are located in the westernmost part of the mapped region just north and northeast of the Caloris impact basin. The strongest single anomaly group lies over a smooth plains unit that extends northward from Caloris. A second anomaly lies on the Odin Formation, interpreted as primary Caloris ejecta. A third broad anomaly also lies over a smooth plains unit, Suisei Planitia. Although many smooth plains on Mercury may have a volcanic origin, a subset of these plains is concentrated around Caloris and could have a dominantly impact origin. It is therefore proposed that many of the Mercurian anomaly sources consist of impact basin ejecta materials.

1. Introduction

The NASA Mercury Surface, Space ENvironment, GEochemistry, and Ranging (MESSENGER) Discovery mission has been an unqualified success and has transformed our understanding of the innermost planet in many ways [e.g., *Denevi and Ernst*, 2011]. Recently, *Johnson et al.* [2015] have reported convincing evidence for the detection of crustal magnetism on Mercury, making it the fourth body in the solar system (after Earth, Moon, and Mars) with this distinction. Their initial interpretation of Mercury's crustal magnetism primarily considered "magnetized intrusive material and magnetization contrasts across deep-seated crustal structures (e.g., faults)" as possible sources of the magnetic anomalies. However, Mercury has many similarities to the Moon for which an impact-related origin of most crustal magnetic anomaly sources has been inferred [e.g., *Hood et al.*, 2001, 2013; *Richmond et al.*, 2003; see also *Wieczorek et al.*, 2012]. Further investigation of the Mercurian crustal anomaly sources and their origin is therefore needed.

For this purpose, an approximate map at constant altitude of part of Mercury's crustal magnetic field is constructed here using an equivalent source dipole (ESD) technique. The map covers a midlatitude section of the Northern Hemisphere, and only calibrated MESSENGER magnetometer measurements that were archived in the Planetary Data System (PDS) as of early October 2015 are considered. The mapping method and results are described in section 2. A discussion of correlations with surface geology and topography is given in section 3, and a brief review of relevant lunar results is given in section 4. Conclusions are given in section 5.

2. Mapping Methods and Results

Although the MESSENGER Mercury orbital mission extended from 18 March 2011 until its impact on the surface on 30 April 2015, periapsis altitudes prior to 2014 were too high for detection of crustal magnetic fields. Only in August of 2014 did periapsis altitudes dip well below 100 km allowing detection of magnetic fields that were clearly of crustal origin [Johnson et al., 2015]. Here we consider only calibrated magnetometer measurements extending through 17 September 2014, which were archived in the PDS as of early October 2015.

Because of the high eccentricity and orientation of the MESSENGER orbit, the spacecraft altitude on a given near-polar orbit was a minimum near 65°N and increased rapidly over distances of only 15° to 20° of latitude. Altitudes less than ~100 km were typically reached at latitudes between approximately 50°N and 80°N. Figure 1a plots surface tracks within this latitude range for 78 orbits covering the period from 23 August to 17 September 2014. Figure 1b maps the mean spacecraft altitude along these orbit tracks. During the last

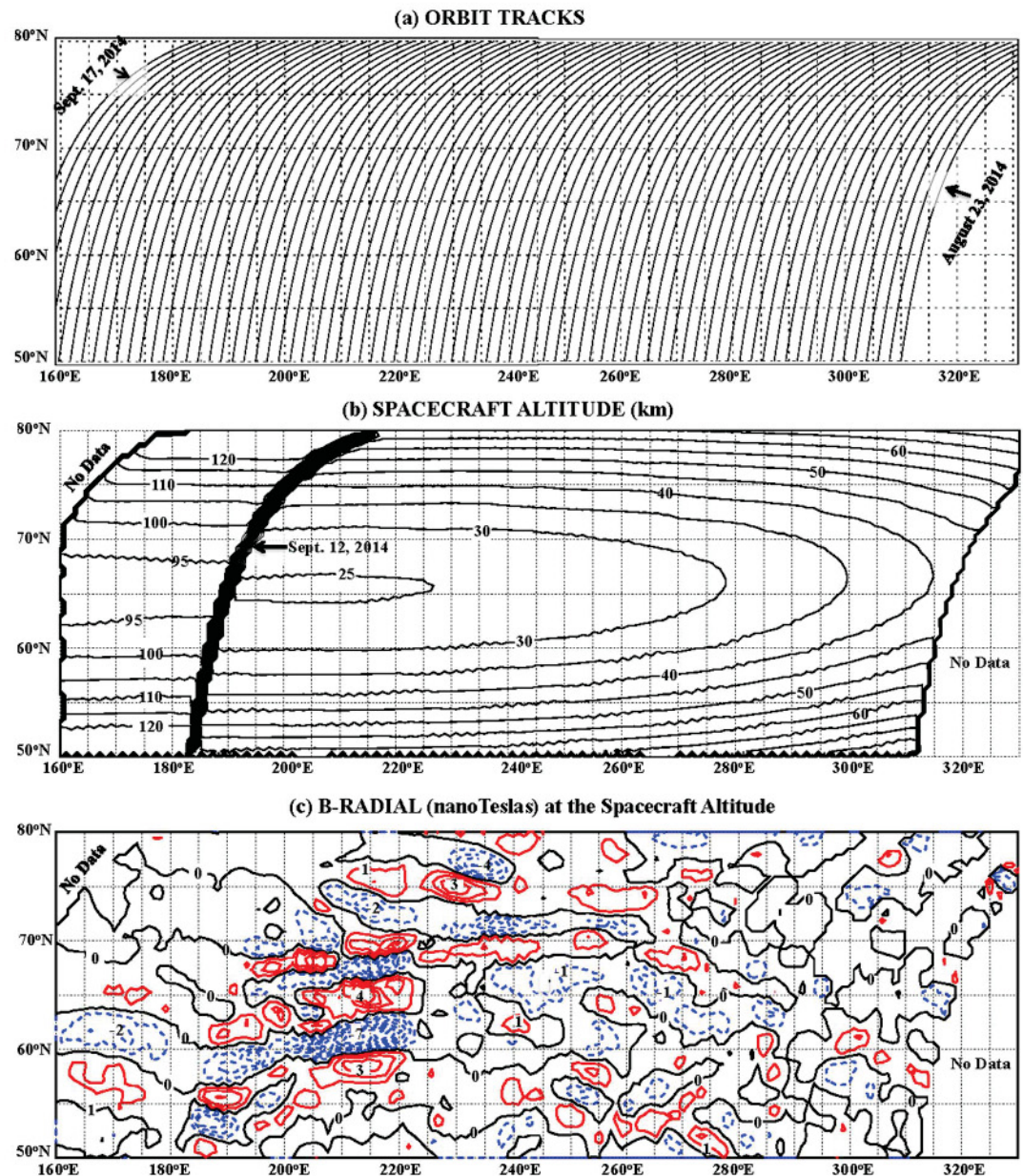


Figure 1. Summary of the selected MESSENGER data: (a) orbit tracks, (b) spacecraft altitude, and (c) radial magnetic field intensity at the spacecraft altitude. In Figure 1c, the contour interval is 1 nT and negative dashed contours are blue; positive contours are red. Time increases from right to left.

part of August and the first 10 days of September, the periapsis altitude decreased gradually from 40 to about 25 km. However, on 12 September, an orbit correction was applied which resulted in a sudden increase in the periapsis altitude from 24.8 km on one orbit to 93.9 km on the next. As seen in the figure, all measurements thereafter were at the higher altitude.

Figure 1c maps the approximate crustal radial field component at the spacecraft altitude shown in Figure 1b. The radial field component is specifically considered because it is usually less affected by high-frequency external field noise than the tangential field components. To produce this map, it was necessary to (a) filter the magnetic field component time series to minimize longer-wavelength contributions from the core field or slowly varying external fields, (b) edit the filtered time series to eliminate periods that were affected by high-frequency external field noise, and (c) sort the remaining measurements into bins and two-dimensionally filter the binned data to produce an equally spaced array suitable for contour mapping.

The filtering and editing of individual orbit data were accomplished in a series of steps. First, for a given orbit, only measurements obtained below a specified minimum altitude (e.g., 100 km) were considered. Second, the field component time series were detrended by least squares fitting and removing a cubic polynomial. This eliminated much, but not all, of longer-wavelength fields that could be of noncrustal origin. To ensure that remaining noncrustal fields were minimized, deviations from the 5° (latitude) running means of the detrended time series were then calculated. One degree of latitude on Mercury is about 43 km so only wavelengths less than roughly 215 km were accepted. A similar high-pass filtering technique was applied by Johnson *et al.* [2015]. Editing of the residuals was accomplished by producing stack plots of the individual field component deviations on a series of orbits. Repetition of field patterns on successive orbits identified periods when dominantly crustal fields were being measured. Remaining periods were characterized by high-frequency noise and were edited out of the time series. Finally, the orbital measurements were sorted into 0.5° latitude by 1° longitude bins and were smoothed once using a 5 by 5 bin boxcar filter.

For most of the selected 78 orbits little or no editing was necessary. However, during the last week of August, high-frequency external field fluctuations were present for many orbits at latitudes $>65^\circ$, rendering the measurements unsuitable for estimation of crustal fields. The radial field component amplitude was therefore set to zero within affected intervals. The net consequence is that, at longitudes $>280^\circ\text{E}$, the resulting field maps have greatly reduced sensitivity at latitudes $>65^\circ\text{N}$.

As seen in Figure 1c, radial field component anomalies are present across much of the map, especially at longitudes near 210°E where periapsis altitudes reached a minimum of less than 25 km. However, weak anomalies are also present near 170°E where the periapsis altitude was about 93 km (also noted by Johnson *et al.*), as verified by stack plots of the filtered measurements. Given the rapid decay of crustal fields with altitude, it is therefore possible or likely that these anomalies are stronger than those near 210°E . Moreover, the spacecraft altitude varies with latitude by as much as a factor of 2 at a given longitude. For these reasons, a map at the MESSENGER spacecraft altitude is not ideal for analysis of correlations with surface geology.

One approach toward applying crustal field measurements at disparate altitudes to construct an approximate map at constant altitude is the equivalent source dipole (ESD) technique [Mayhew, 1979; von Frese *et al.*, 1981; Purucker *et al.*, 2000; Langlais *et al.*, 2004]. In its simplest form, this involves assuming that the sources of the crustal field can be represented as an array of point magnetic dipoles on a spherical surface with some specified orientation, horizontal separation, and depth beneath the planetary mean surface. The amplitudes of the individual dipole moments are then adjusted until a minimum variance between the observed magnetic field and the model magnetic field is obtained. In principle, only one observed field component needs to be considered since the crustal field is, by definition, a potential field. As noted above, this is usually the radial field component since it is often less affected by external field noise and is typically somewhat stronger than the horizontal components for a given anomaly. While the resulting solution for the effective crustal magnetization distribution is nonunique (because of the specified orientation), the final array of magnetic dipoles can be used to calculate the approximate field at a constant altitude. The solution is approximate because of the remaining external field noise in the magnetic field residuals, which affects the estimated dipole moment amplitudes. Only upward or moderate downward continuation from the spacecraft altitude is therefore advisable to avoid amplification of the noise component.

As indicated schematically in Figure 2a, an equivalent source model was assumed in the form of an array of 86 by 31 (2666) vertically oriented magnetic dipoles separated by 1° in latitude and 2° in longitude covering longitudes from 160°E to 330°E . The array was placed on a spherical surface at a depth of 20 km below the mean Mercury radius with all dipole moment amplitudes initially set to $+1\text{ G km}^3$ (10^{12} A m^2). To increase computational efficiency, the array was divided into a series of eight overlapping 30° longitude sectors (160°E to 190°E , 180° to 210°E , etc.). Also, the number of data points along a given orbit track between 50°N and 80°N was reduced from ~ 7100 to 300 by calculating 0.1° latitude averages. Within each sector, a minimum variance fit of the 16 by 31 array of dipole moments to the 0.1° averaged measurements along the orbit tracks was obtained via an iterative procedure. Specifically, if the model radial field component in a given 1° latitude by 2° longitude bin was less (greater) than the nearest observed radial field component at the spacecraft altitude, then the amplitude of the dipole moment for that bin was incremented positively (negatively) by 0.1 G km^3 . After each loop through all 496 dipoles, the total RMS deviation was calculated. Convergence to an approximate solution was found to occur typically after about 50 iterations. Final RMS deviations in a given sector ranged from 0.21 to 0.33 nT, and the overall correlation coefficient between the observed and

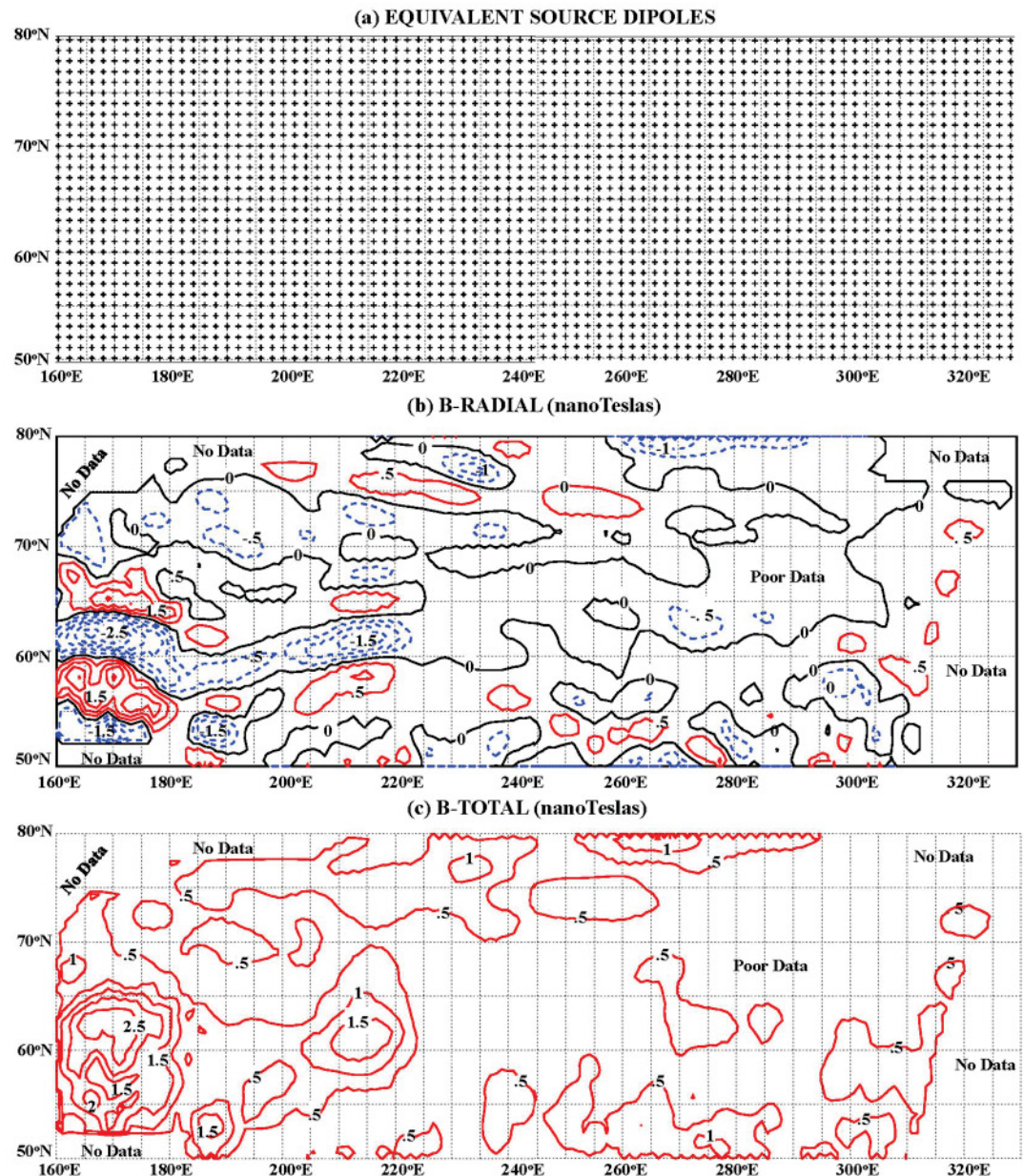


Figure 2. Equivalent source dipole modeling results: (a) assumed source dipole distribution, (b) radial magnetic field intensity at 80 km altitude calculated from the ESD solution, and (c) magnetic field magnitude at 80 km. The contour interval for Figures 2b and 2c is 0.5 nT.

model radial field components along the original orbit tracks sampled at 0.5° latitude resolution was $R = 0.92$ (> 4000 data points).

The complete array of 86 by 31 model dipoles was then obtained from the overlapping individual sector solutions. To avoid edge effects, results from the last 5° of the first sector (160°E to 190°E) and from the first 5° of the second sector (180°E to 210°E) were discarded. This was repeated for the remaining sectors. Finally, the model magnetic field components were calculated along the original 78 orbit tracks at a constant altitude. Figure 2b shows the model crustal radial field component at an altitude of 80 km. This mean altitude was chosen because it is an intermediate between the spacecraft altitude after 12 September (> 93 km) and that before this date (25 to 70 km). Choosing a mean altitude significantly lower than 80 km (e.g., 40 km) results in large amplifications of external field noise in the western part of the map where the spacecraft altitude was high. Even at 80 km altitude, external field noise was excessively amplified when the spacecraft altitude was

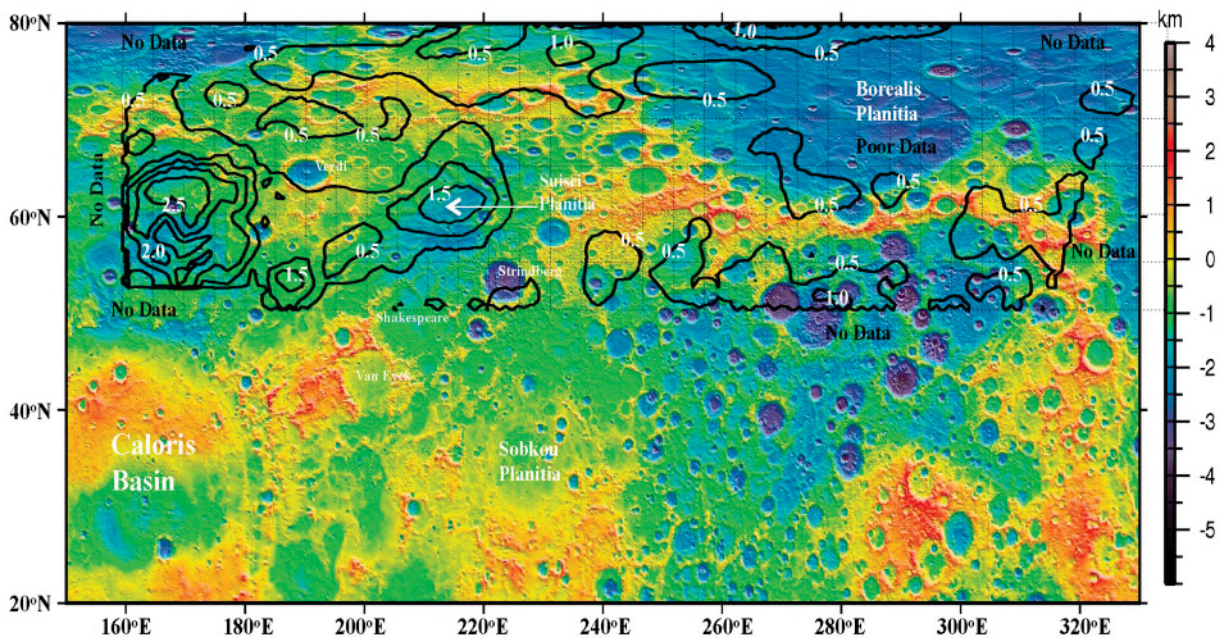


Figure 3. Superposition of the field magnitude map at 80 km altitude of Figure 2c onto a MESSENGER Laser Altimeter shaded relief map (see the text). Major geologic features are labeled, and areas with little or no data are indicated.

higher than 120 km, as it was after 12 September at latitudes $>75^{\circ}\text{N}$ and $<52^{\circ}\text{N}$. These data were therefore not mapped as indicated by “No Data” labels in the western part of the map. As mentioned above, the north-eastern part of the map is not reliable due to excessive external field noise for many orbits during the last week of August. “No Data” and “Poor Data” labels are therefore also added to the affected regions.

The resulting map is not strongly dependent on the choice of an exactly radial orientation for the dipole array. Separate calculations for a dipole array with assumed orientations up to $\sim 70^{\circ}$ from radial yield similar results (see Figure S1 in the supporting information for a map assuming an orientation of 45° from radial). Beyond about 70° , convergence to a solution becomes increasingly difficult because the radial field component is being fitted to an array of nearly horizontal dipoles. Results are somewhat more sensitive to the choice of the depth of the dipole array. Based on trial calculations, it was found that a depth of 20 km yields a minimum total RMS deviation of the model radial field component from the observed radial field component. Depths in the range of 10 to 30 km yield comparable results (see Figure S2 for a map assuming a depth of 10 km), but RMS deviations increase significantly outside of this range.

Comparing Figure 2b with Figure 1c, it is clear that continuation to a constant altitude is valuable for mapping the true distribution of Mercurian crustal fields, given the MESSENGER orbit characteristics. In Figure 2b, most strong anomalies (smoothed amplitudes ≥ 1.5 nT at 80 km altitude) are in the westernmost part of the mapped region. The strongest group of anomalies (> 2 nT) is centered near 170°E where the spacecraft altitude was more than 93 km. The ESD technique also allows estimation of the horizontal field components and the field magnitude at constant altitude. Figure 2c plots the model field magnitude. At least six anomalies or anomaly groups can be identified with smoothed amplitudes at 80 km ≥ 1 nT.

3. Correlations With Surface Geology/Topography

Figure 3 is a superposition of (a) the total field map of Figure 2c, (b) a Northern Hemisphere elevation model derived by the mission team from MESSENGER Laser Altimeter (MLA) data (G. Neumann, priv. comm., 2015), and (c) a monochrome mosaic produced by the team from MESSENGER Dual Imaging System data (messenger.jhuapl.edu). Also identified in the figure are major geologic features including the Caloris impact basin, the Shakespeare impact basin, a large region of lower elevation known as Borealis Planitia, and another region of lower elevation known as Suisai Planitia.

Although the Caloris basin is outside the mapped magnetic field area, a tendency for field amplitudes to increase in the area north and northeast of Caloris is evident. In the central and southeastern part of the

magnetic field map, where the data quality is good, anomalies are clearly weaker than they are westward of 230°E. Fields also appear to be relatively weak over Borealis Planitia, which is currently interpreted as a volcanic lava plain [Denevi *et al.*, 2013]. However, this is an area of poor data quality as discussed above so a confirmation of weak fields over Borealis Planitia must await further mapping. If weak fields are ultimately confirmed, then Borealis Planitia could represent an analog to the lunar maria, which is also magnetically very weak [e.g., Hood *et al.*, 2001; Halekas *et al.*, 2001]. One strong but smaller-scale anomaly in the western region is centered at about 187°E, 53°N, an area of moderate elevation. A comparison with available geologic maps [Guest and Greeley, 1983] shows that this location is over the Odin Formation, interpreted as primary Caloris basin ejecta.

As reported originally by Johnson *et al.* [2015], the strongest anomalies in the mapped region tend to be associated with smooth plains. One strong and broad anomaly occurs over Suisei Planitia, a lower elevation, smooth plains unit northeast of Caloris. The strongest anomaly group occurs over another unnamed low-elevation, smooth planitia that extends radially northward from Caloris (see also Figure S3).

As discussed by Denevi *et al.* [2013], a majority of Mercurian smooth plains appear to have a volcanic origin, including those such as Borealis Planitia over the northern lowlands. However, an impact-related origin for some of these plains, including Suisei Planitia and the unnamed planitia north of Caloris, cannot be ruled out. The latter plains are part of an annulus of similar plains concentrated around Caloris [see Denevi *et al.*, 2013, Figure 1]. As discussed in detail by the latter authors, the relatively sparse crater population of these plains suggests that they are younger than Caloris, which would favor a volcanic origin [e.g., Strom *et al.*, 2008; Fassett *et al.*, 2009]. However, the circum-Caloris plains have a number of characteristics in common with the Odin Formation, which is more clearly interpreted as Caloris basin ejecta. These include a relatively low reflectance and a similar color to Caloris rim deposits. Also, no impact craters that are clearly younger than Caloris itself but older than its volcanically resurfaced interior have been found on the circum-Caloris smooth plains [Wilhelms, 1976]. It is therefore conceivable that the cratering frequency on the smooth plains is biased downward in some way. For example, Denevi *et al.* note that near-field secondary cratering immediately following the Caloris impact could have led to a higher population of craters on the Caloris rim than on the adjacent ejecta field. Also, different physical properties of the smooth plains material immediately after deposition may have led to different crater sizes for a given secondary impactor size than elsewhere.

Moderate-amplitude (~ 1 nT at 80 km) anomalies are also seen at about 233°E, 77°N; 265°E, 78°N; and 275°E, 52°N. The first and third of these occur over intermediate plains material, interpreted by Guest and Greeley [1983] and Grolier and Boyce [1984] as having an uncertain origin, possibly consisting of a combination of impact basin and crater ejecta as well as some volcanic materials. On the other hand, McGill and King [1983] interpret the same unit as probably basaltic lava flows. Crater densities suggest an age that is older than that of smooth plains such as Suisei Planitia. The second occurs over smooth plains of northeastern Borealis Planitia, which is elsewhere apparently weak magnetically, as discussed above.

4. Relation to Lunar Crustal Magnetism

In view of the association of Mercurian strong magnetic anomalies with smooth plains, it is useful to consider several results of prior studies of lunar crustal magnetism. Of the four Apollo landings that deployed surface magnetometers, the strongest surface fields (up to 327 nT) were measured along a traverse near the Apollo 16 landing site in an area dominated geologically by a smooth plains unit, the Cayley Formation [Dyal *et al.*, 1974]. Prior to Apollo, the Cayley was interpreted as volcanic in origin [e.g., Milton, 1972]. But shortly after the Apollo 16 landing, it was found to instead be composed of impact breccias [Eggleton and Schaber, 1972]. The measured magnetic field intensity and orientation along the Apollo 16 surface traverse varied widely implying localized, near-surface sources. Early sample analyses showed that highland breccias contain relatively more metallic iron remanence carriers and stronger magnetizations than pristine igneous rocks (mare basalts and anorthosites) [Strangway *et al.*, 1973a; Fuller and Cisowski, 1987]. More recently, Rochette *et al.* [2010] have found that the enhanced metallic iron content of lunar breccias is due at least in part to the addition of meteoritic metal during impacts.

For these reasons, Strangway *et al.* [1973b] originally proposed that impact ejecta materials such as the Cayley Formation are the most probable sources of crustal magnetic anomalies detected from lunar orbit. In support of this possibility, analyses of low-altitude Apollo 16 subsatellite magnetometer data found evidence for associations of orbital anomalies with both the Cayley Formation and the Fra Mauro Formation south

of the Imbrium impact basin [Hood *et al.*, 1979]. The Cayley Formation was found to be the single geologic unit that correlates best with crustal magnetic anomalies on the lunar nearside [Halekas *et al.*, 2001]. During the post-Apollo period, the Cayley plains, as well as other similar smooth plains units, were interpreted as primary and secondary impact basin ejecta debris that were preferentially emplaced in low-lying areas [Muehlberger *et al.*, 1972; Wilhelms, 1987]. Later analyses of global Lunar Prospector magnetometer data found that the strongest single anomaly on the lunar nearside occurs adjacent to the Apollo 16 landing site over the Descartes highlands, interpreted as primary impact basin ejecta [Halekas *et al.*, 2001; Richmond *et al.*, 2003]. Overall, these results led to the current leading (but not yet fully accepted) hypothesis that basin ejecta materials are the main sources of strong lunar crustal magnetic anomalies [e.g., Hood *et al.*, 2001, 2013]. It has also been proposed that many strong anomalies on the farside are associated with ejecta from the impact of an iron-rich asteroid that produced the South Pole-Aitken basin [Wieczorek *et al.*, 2012]. In principle, such ejecta materials may have acquired their magnetizations via either thermoremanence or shock remanence, depending on their thermal and shock histories [Gattacceca *et al.*, 2010].

As originally pointed out by Wilhelms [1976], Mercurian smooth plains bear many morphological similarities to lunar light plains such as the Cayley Formation. He therefore proposed that at least some of these plains on Mercury may have an impact-related origin involving fluidized basin ejecta deposition. The current realization that the circum-Caloris plains are associated with strong magnetic anomalies combined with the association of lunar magnetic anomalies with smooth plains having a known impact origin therefore adds weight to Wilhelms' proposal [Hood, 2015].

5. Conclusions

The ESD technique is valuable for producing an approximate map of Mercurian crustal magnetic anomalies at a constant altitude from the MESSENGER magnetometer data. Application of this technique to a selected set of data from August to September of 2014 shows that the strongest anomalies are present in the westernmost part of the mapped region north and northeast of the Caloris impact basin. An association of these anomalies with Caloris is supported by the occurrence of one anomaly over the Odin Formation, interpreted as primary Caloris basin ejecta, and the occurrence of several broad anomalies over circum-Caloris smooth plains, one of which extends radially northward from Caloris. The latter plains may have an impact-related origin by analogy with the lunar Cayley plains, which have a known impact origin and which are also associated with strong lunar crustal magnetic anomalies. Overall, these results are consistent with the hypothesis that basin ejecta materials are the sources of relatively strong magnetic anomalies on both the Moon and Mercury. At least on the Moon, these materials are known to contain more metallic iron remanence carriers than igneous materials [Rochette *et al.*, 2010]. They may have acquired their magnetizations via either shock or thermoremanence after deposition [Gattacceca *et al.*, 2010]. On Mercury, if the magnetization was primarily thermoremanent during slow cooling, then a steady magnetizing field consistent with an unmodified early core dynamo is implied [Johnson *et al.*, 2015]. However, if the magnetization was primarily acquired via shock, a transient magnetizing field associated with the impact process (e.g., a modified early core dynamo field or an amplified solar wind field) cannot be ruled out.

Acknowledgments

The MESSENGER calibrated magnetometer data are available from the Planetary Plasma Interactions node of the NASA Planetary Data System (ppi.pds.nasa.gov). Useful correspondence with Catherine Johnson and Brett Denevi is appreciated. Greg Neumann kindly provided the background MLA image for Figure 3. Thanks to Jerome Gattacceca and an anonymous reviewer for helpful comments and criticisms that improved the paper.

References

- Denevi, B., and C. Ernst (2011), MESSENGER: Revealing Mercury's secrets, paper presented at Lunar and Planetary Information Bulletin No. 127, Lunar and Planetary Institute, Universities Space Research Association, pp. 2–5, Houston, Tex., Dec.
- Denevi, B., et al. (2013), The distribution and origin of smooth plains on Mercury, *J. Geophys. Res. Planets*, 118, 891–907, doi:10.1002/jgre.20075.
- Dyal, P., C. W. Parkin, and W. D. Daily (1974), Magnetism and the interior of the Moon, *Rev. Geophys. Space Phys.*, 12, 568–591.
- Eggleton, R. E., and G. G. Schaber (1972), Cayley formation interpreted as basin ejecta, in *Apollo 16 Preliminary Science Report, Spec. Publ. SP-315*, pp. 29–7–29–16, NASA, Washington, D. C.
- Fassett, C. I., J. W. Head, D. T. Blewett, C. R. Chapman, J. L. Dickson, S. L. Murchie, S. C. Solomon, and T. R. Watters (2009), Caloris impact basin: Exterior geomorphology, stratigraphy, morphometry, radial sculpture, and smooth plains deposits, *Earth Planet. Sci. Lett.*, 285, 297–308.
- Fuller, M., and S. Cisowski (1987), Lunar paleomagnetism, in *Geomagnetism*, vol. 2, edited by J. Jacobs, pp. 307–456, Academic Press, Orlando, Fla.
- Gattacceca, J., M. Boustie, L. Hood, J.-P. Cuq-Lelandais, M. Fuller, N. S. Bezaeva, T. de Resseguier, and L. Berthe (2010), Can the lunar crust be magnetized by shock: Experimental groundtruth, *Earth Planet. Sci. Lett.*, 299, 42–53.
- Grolier, M. J., and J. M. Boyce (1984), Geologic map of the Borealis Region of Mercury, *U.S. Geol. Surv. Map I-1660*.
- Guest, J. E., and R. Greeley (1983), Geologic map of the Shakespeare Quadrangle of Mercury, *U.S. Geol. Surv. Map I-1408*.
- Halekas, J. S., D. L. Mitchell, R. P. Lin, S. Frey, L. Hood, M. Acuña, and A. B. Binder (2001), Mapping of lunar crustal magnetic fields using Lunar Prospector electron reflectometer data, *J. Geophys. Res.*, 106, 27,841–27,852.
- Hood, L. L. (2015), Mercury and the Moon, *Science*, 349, 1459.

- Hood, L. L., P. J. Coleman Jr., C. T. Russell, and D. E. Wilhelms (1979), Lunar magnetic anomalies detected by the Apollo subsatellite magnetometers, *Phys. Earth Planet. Int.*, **20**, 291–311.
- Hood, L. L., A. Zakharian, J. Halekas, D. L. Mitchell, R. P. Lin, M. H. Acuña, and A. B. Binder (2001), Initial mapping and interpretation of lunar crustal magnetic anomalies using Lunar Prospector magnetometer data, *J. Geophys. Res.*, **106**, 27,825–27,839.
- Hood, L. L., N. C. Richmond, and P. D. Spudis (2013), Origin of strong lunar magnetic anomalies: Further mapping and examinations of LROC imagery in regions antipodal to young large impact basins, *J. Geophys. Res. Planets*, **118**, 1265–1284, doi:10.1002/jgre.20078.
- Johnson, C. L., et al. (2015), Low-altitude magnetic field measurements by MESSENGER reveal Mercury's ancient crustal field, *Science*, **348**, 892–895, doi:10.1126/science.aaa8720.
- Langlais, B., M. E. Purucker, and M. Mandea (2004), Crustal magnetic field of Mars, *J. Geophys. Res.*, **109**, E02008, doi:10.1029/2003JE002048.
- Mayhew, M. A. (1979), Inversion of satellite magnetic anomaly data, *J. Geophys.*, **45**, 119–128.
- McGill, G. E., and E. A. King (1983), Geologic map of the Victoria Quadrangle of Mercury, *U.S. Geol. Surv. Map I-1409*.
- Milton, D. J. (1972), Geologic map of the Descartes region of the Moon, Apollo 16 pre-mission map, *U.S. Geol. Surv. Map I-742*.
- Muehlberger, W. R., et al. (1972), Preliminary geologic investigation of the Apollo 16 landing site, in *Apollo 16 Preliminary Science Report*, Spec. Publ. 315, pp. 6–1–6–81, NASA, Washington, D. C.
- Purucker, M., D. Ravat, H. Frey, C. Voorhies, T. Sabaka, and M. Acuña (2000), An altitude-normalized magnetic map of Mars and its interpretation, *Geophys. Res. Lett.*, **27**, 2449–2452.
- Richmond, N. C., L. Hood, J. Halekas, D. Mitchell, R. Lin, M. Acuña, and A. Binder (2003), Correlation of a strong lunar magnetic anomaly with a high albedo region of the Descartes mountains, *Geophys. Res. Lett.*, **30**(7), 1395, doi:10.1029/2003GL016938.
- Rochette, P., J. Gattacceca, A. V. Ivanov, M. A. Nazarov, and N. S. Bezaeva (2010), Magnetic properties of lunar materials: Meteorites, Luna and Apollo returned samples, *Earth Planet. Sci. Lett.*, **292**, 383–391.
- Strangway, D. W., W. Gose, G. Pearce, and R. McConnell (1973a), Magnetism and the history of the Moon, in *Magnetism and Magnetic Materials—1972*, edited by C. Graham Jr. and J. Rhyne, pp. 1178–1187, Am. Inst. of Phys., New York.
- Strangway, D. W., H. Sharpe, W. Gose, and G. Pearce (1973b), Lunar magnetic anomalies and the Cayley Formation, *Nature*, **246**, 112–114.
- Strom, R. G., C. R. Chapman, W. J. Merline, S. C. Solomon, and J. W. Head (2008), Mercury cratering record viewed from MESSENGER's first flyby, *Science*, **321**, 79–81.
- von Frese, R. R. B., W. J. Hinze, and L. W. Braille (1981), Spherical Earth gravity and magnetic anomaly analysis by equivalent point source inversion, *Earth Planet. Sci. Lett.*, **53**, 69–83.
- Wieczorek, M. A., B. P. Weiss, and S. T. Stewart (2012), An impactor origin for lunar magnetic anomalies, *Science*, **335**, 1212–1215.
- Wilhelms, D. E. (1976), Mercurian volcanism questioned, *Icarus*, **28**, 551–558.
- Wilhelms, D. E. (1987), The geologic history of the Moon, *U.S. Geol. Surv. Prof. Pap.*, **1348**, U.S. Gov. Print. Off., Washington, D. C.